

Unraveling mitotic protein networks by 3D multiplexed epitope drug screening

Lorenz Maier^{1,2}, Stefan Kallenberger^{1,2}, Katharina Jechow¹, Marcel Waschow¹, Roland Eils^{1,2*}, Christian Conrad^{1*}

¹German Cancer Research Center (DKFZ), Theoretical Bioinformatics Division, Im Neuenheimer Feld 267, 69120 Heidelberg, Germany

²Heidelberg University, Institute for Pharmacy and Molecular Biology (IPMB), Bioinformatics and Functional Genomics Department, Im Neuenheimer Feld 364, 69120 Heidelberg, Germany

* Corresponding authors. RE: r.eils@dkfz.de CC: c.conrad@dkfz.de

Keywords: Multiplexed immunostaining, 3D cell culture, protein-protein interactions, mitosis

Three-dimensional protein localization intricately determines the functional coordination of cellular processes. The complex spatial context of protein landscape has been assessed by multiplexed immunofluorescent staining¹⁻³ or mass spectrometry⁴, applied to 2D cell culture with limited physiological relevance⁵ or tissue sections. Here, we present **3D SPECS**, an automated technology for **3D** Spatial characterization of **P**rotein **E**xpression **C**hanges by microscopic **S**creening. This workflow encompasses iterative antibody staining of proteins, high-content imaging, and machine learning based classification of mitotic states. This is followed by mapping of spatial protein localization into a spherical, cellular coordinate system, the basis used for model-based prediction of spatially resolved affinities of various mitotic proteins. As a proof-of-concept, we mapped twelve epitopes in 3D cultured epithelial breast spheroids and investigated the network effects of mitotic cancer drugs with known limited success in clinical trials⁶⁻⁸. Our approach reveals novel insights into spindle fragility and global chromatin stress, and predicts unknown interactions between proteins in specific mitotic pathways. **3D SPECS's** ability to map potential drug targets by multiplexed immunofluorescence in 3D cell cultured models combined with our automatized high content assay will inspire future functional protein expression and drug assays.

Iterative antibody labeling overcomes the spectral limit of total number of fluorescent antibodies that can be applied simultaneously to individual cells^{1,3}. We successfully extend this technique of chemically bleached fluorescently labeled antibodies, to 3D cell cultured spheroids in Matrigel⁹ combined with drug treatment (see Supplementary Table 1). Our setup (**Fig. 1a**) uses confocal laser scanning microscopy together with automated pre-screen classification by machine learning and motorized in-built micro pipetting robot to identify and comprehensively stain mitotic phases. Naturally, mitotic cells self-organize, structure and typically segregate in different orientations, rendering a direct comparison of different data sets impossible. To overcome this limitation, we propose a novel representation named **SpheriCell** for spatial alignment of subcellular images. It infers a spherical coordinate system of the cellular space, using the spindle axis perpendicular to the metaphase plate to define the orientation of the vertical axis, while the metaphase plate defines the equatorial plane. Within this spherical coordinate system, protein concentrations are measured as 3D partitions in three symmetrical sets of spherical sectors and six shells. For enhanced visualization, mean values of 3D partitions are projected onto a two-dimensional longitudinal plane (**Fig. 1b**). Hence, we screened 6,272 image stacks, identified 1,217 mitotic events resulting in 284,778 mean intensity values of 3D partitions. We illustrate differences between tumorigenic and non-tumorigenic 3D cell lines in more physiological conditions still accessible by high-throughput screening⁵. The applied human epithelial MCF10 breast cancer progression model compares near-diploid cell line MCF10A¹⁰ forming polarized spheroids¹¹ with the tumorigenic line MCF10CA, which bear activating mutations of *HRAS* and *PIK3CA*, amplified *MYC*, but wild-type *TP53*¹⁰.

Using **3D SPECS**, we first studied sub-cellular differences in protein localizations in the tumorigenic and non-tumorigenic 3D cell lines distinguishing between the cell cycle states metaphase and segregation. Here we assessed co-localization affinities of proteins and their preferred localization to subcellular compartments by our mathematical modeling approach. We thus unraveled network-wide treatment effects on mitotic spindle organization, spindle assembly checkpoint (SAC), and complementary cell fate indicators. The spindle assembly checkpoint (SAC) control includes e.g. the chromosome passenger complex (CPC) comprising BIRC5, Borealin, INCENP, and Aurora B¹², which inhibit anaphase promoting complex (APC/C) most efficiently through mitotic checkpoint complex (MCC) containing BUB1 β (BUBR1)¹³. Failures in these checkpoints can lead to disruption of mitosis and subsequent autophagic or necrotic events.

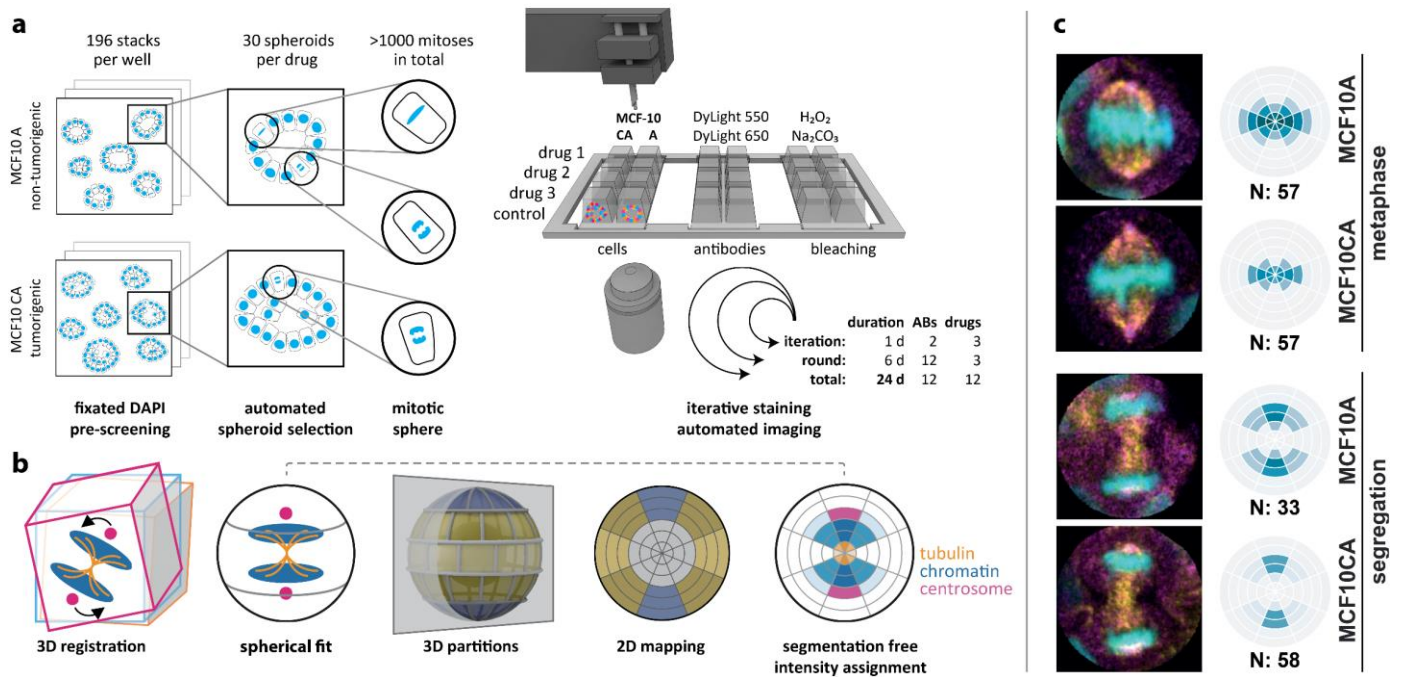


Figure 1 Workflow of iterative antibody labeling. (a) After 48h drug treatment, MCF10A and MCF10CA cells were fixed and DAPI stained. Pre-screening comprised 196 image stacks per well to automatically select 30 spheroids that each showed at least one mitosis. At each round, selected positions for three drug treatments plus control were stained, imaged, and bleached in six iterations with two antibodies each. Within 24 days, we acquired 3D stacks of twelve antibodies on twelve drug treatments and two cell lines. (b) **SpheriCell** visualization: Stacks were 3D registered and a sphere was fitted to each cell division area, which was partitioned into three symmetrical sets of spherical sectors and six shells. Spherical 3D localization can be visualized by a longitudinal cut resulting in a 2D polar grid that contains projected mean values of 3D partitions. Moreover, cell poles are not distinguishable, so the results are centrally symmetric. Localization of mitotic proteins can be intuitively determined from the 2D projected partitions as exemplified by tubulin, chromatin, and centrosomal regions. Color intensities reflect normalized, mean protein concentrations in each bin. (c) Example images and DAPI binning. Distinguished between MCF10A and MCF10CA, and metaphase and segregation spanning ana- and telophase. DAPI (cyan), γ -Tubulin (magenta), and β -Tubulin (yellow). Example images were rotated manually. ABs: antibodies; N: number of mitoses contributing to mean values.

We confirmed known localizations of cellular proteins and known mitotic checkpoints for untreated cells as described before^{12–21}, supporting the utility of **3D SPECS (Fig. 2a)**. MCF10CA staining patterns resembled those of MCF10A, showing a slightly reduced average DAPI signal due to increased cell size. Highest protein concentration increases were observed for γ -H2AX and Aurora A, contrasted by a reduction strongest for γ -Tubulin (**Fig. 2b**). Increased levels of γ -H2AX¹⁶, a marker for double strand breaks, may reflect higher chromosomal stress. Higher intensity levels of Aurora A, which is upregulated during mitosis and localizes mostly towards centrosomes¹⁴, in MCF10CA is consistent with previously described effects upon activation of Raf-1²², downstream of the oncogenic RAS pathway.

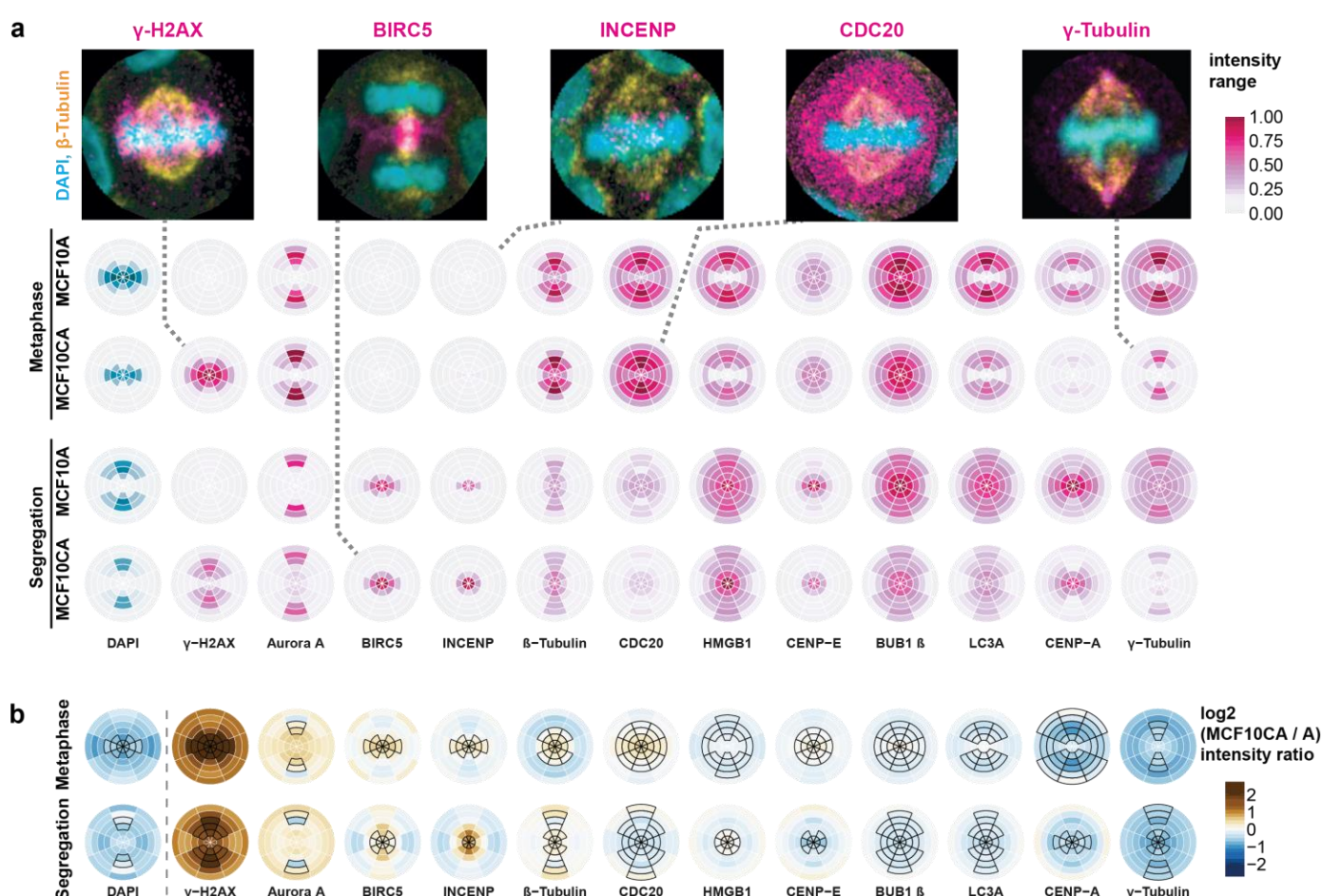


Figure 2 Localization and intensity changes of twelve antibody stainings of untreated MCF10A and MCF10CA cells during metaphase and segregation comprising ana- and telophase. SpheriCell plots depict mean intensity values across all imaging rounds, ordered by decreasing difference between MCF10CA and MCF10A cells. **(a)** Localization of epitopes. Intensity ranges were specific to the antibody and are shown normalized between 0 and 1, effectively across all values of a column in the figure. Distribution patterns generally reflect the localization of individual

proteins described before^{12–21}. Dashed lines connect SpheriCell plots with example images of antibody stainings (magenta), DAPI (cyan), and β -Tubulin (yellow). **(b)** MCF10CA shows altered intensity patterns compared to MCF10A. SpheriCell plots depict differences of log2 transformed fluorescence intensity of MCF10CA and MCF10A [$\log_2(\text{CA}) - \log_2(\text{A})$] for metaphase and segregation, in decreasing order. Black framed partitions indicate intensity distributions in untreated control images. LC3A: microtubule-associated proteins 1A/1B light chain 3A.

We then analyzed the effects of twelve targeted inhibitors on mitotic proteins of dividing MCF10A and MCF10CA cells (**Fig. 3a,b**), specifically on protein concentrations and preferred localizations. To compare spatial distribution patterns of protein intensities, in each cell, 18 subcellular compartments were defined by a combination of six eccentricity shells with three orientations relative to the division plane. In analogy to calculating a center of mass, we specified measures of spatial intensity distributions (**Supplementary Note 1**). **Fig. 3a** visualizes significant concentration fold changes and spatial changes in eccentricity and orientation compared between cell lines, mitotic phases and for inhibitors relative to controls. Notably, comparisons between cell lines showed more pronounced effects on concentration fold changes than on spatial distributions. MCF10CA cells showed significantly higher γ -H2AX and Aurora A concentrations, but lower γ -Tubulin concentrations. Changes in eccentricity and orientation of the localization pattern could be observed in MCF10CA relative to MCF10A cells mostly during metaphase. Obviously, as indicated for the comparison between segregation and metaphase, the mitotic phase strongly influenced the spatial distributions of most observed proteins. Changes in the distribution pattern for DAPI and γ -H2AX reflect the movement of the nucleus towards the cell division axis and to higher eccentricity while the other proteins move closer to the cell division plane.

During segregation, relative to metaphase, both cell lines showed a known decrease in CDC20 concentration²³ and elevated BIRC5 concentrations, whereas the CENP-A was only increased in MCF10A cells. Inhibitors mostly increased the concentrations of several proteins but hardly affected their spatial distributions (**Fig. 3b**). Here, the inhibitions of master regulator AURKB¹² and also Haspin known to be implicated in Aurora B positioning¹² showed a prominent effect across nearly all proteins in MCF10A as well as MCF10CA cells. Moreover, we detected broad effects of increased DNA damage by Topoisomerase II poisoning²⁴. Interestingly, MCF10CA cells appeared to be more sensitive to mitotic spindle interference, reflected by effects on Aurora A and CENP-E. Concordantly, inhibition of Aurora A

affected more proteins in MCF10CA spheroids compared to MCF10A. MCF10CA showed more pronounced effects of PLK1 inhibition. Contrarily, although KIF11 (Eg5) and KIFC1 (HSET) facilitate separation and clustering of centrosomes²⁵, the effects due to inhibition of KIF11 were restricted to MCF10A cells. High natural levels of γ -H2AX intensity in MCF10CA were not increased by our treatments as observed in MCF10A. Also, BIRC5 concentration was affected in MCF10A but not in MCF10CA cells. In contrast to effects on concentrations, the eccentricity and the orientation of distribution patterns were less affected by inhibitions except for Haspin and PLK1 being two notable exceptions.

To study intracellular distributions and localized interactions between proteins, we developed a non-linear model that was calibrated with our partitioned mitotic protein intensity data (**Supplementary Note 1**). To capture interactions between proteins in a simplified manner, the model describes concentrations at steady state for monomers, homo- and heterodimers of all proteins bound to subcellular compartments with first and second order interactions. Affinities of every protein to subcellular compartments, and affinities between proteins were estimated by model fitting. To predict new affinities between proteins, we started by fitting a model of interactions from literature in *Ingenuity Pathway Analysis* (IPA) regarded as ground truth. This initial model was fitted to our untreated control cells. Then, by sequential forward selection, new mutual affinities between proteins were additionally included in the model and pertained if model fits were significantly improved, based on likelihood-ratio testing. **Fig. 3c** visualizes the 19 known interactions overlaid with all 16 additionally predicted mutual affinities. Interestingly, colocalization affinities between species do not necessarily imply functional relations and pathway interactions do not require high affinities. For example, we identified known interactions of γ -Tubulin with CDC20²⁶ as well as known DNA-binding of BIRC5¹² (**Fig. 3c**). While we triggered DNA damage pathways with Topoisomerase II poisoning and inhibition of CHK1²⁷, indications of cell fate could be inferred from double strand break marker γ -H2AX¹⁶, necrosis associated HMGB1¹⁷, and autophagic vesicle marker MAP1LC3A (LC3)¹⁸. BIRC5 was predicted by the model to interact with LC3, which links mitotic surveillance and autophagy pathways¹⁸. The model predicted interactions of γ -H2AX, γ -Tubulin and β -Tubulin with several other proteins, which might indicate indirect interactions with the mitotic spindle or the cytoskeleton. Coefficients describing mutual affinities between proteins are depicted in **Fig. 3d**. Importantly, the fraction of a protein that is localized to a mitotic bin due to mutual interactions with other proteins does not only depend on affinity coefficients but may require high affinities of interacting species to the

respective mitotic bin. Estimated fractions of proteins recruited to subcellular compartments due to mutual interactions with other proteins, as well as estimated affinities to subcellular compartments are shown in **Supplementary Fig. 1**. The highest values of mutual affinities with other proteins were found between CENP-E molecules as described earlier²⁸ and for the newly predicted binding of β -Tubulin to HMGB1 (**Fig. 3d**).

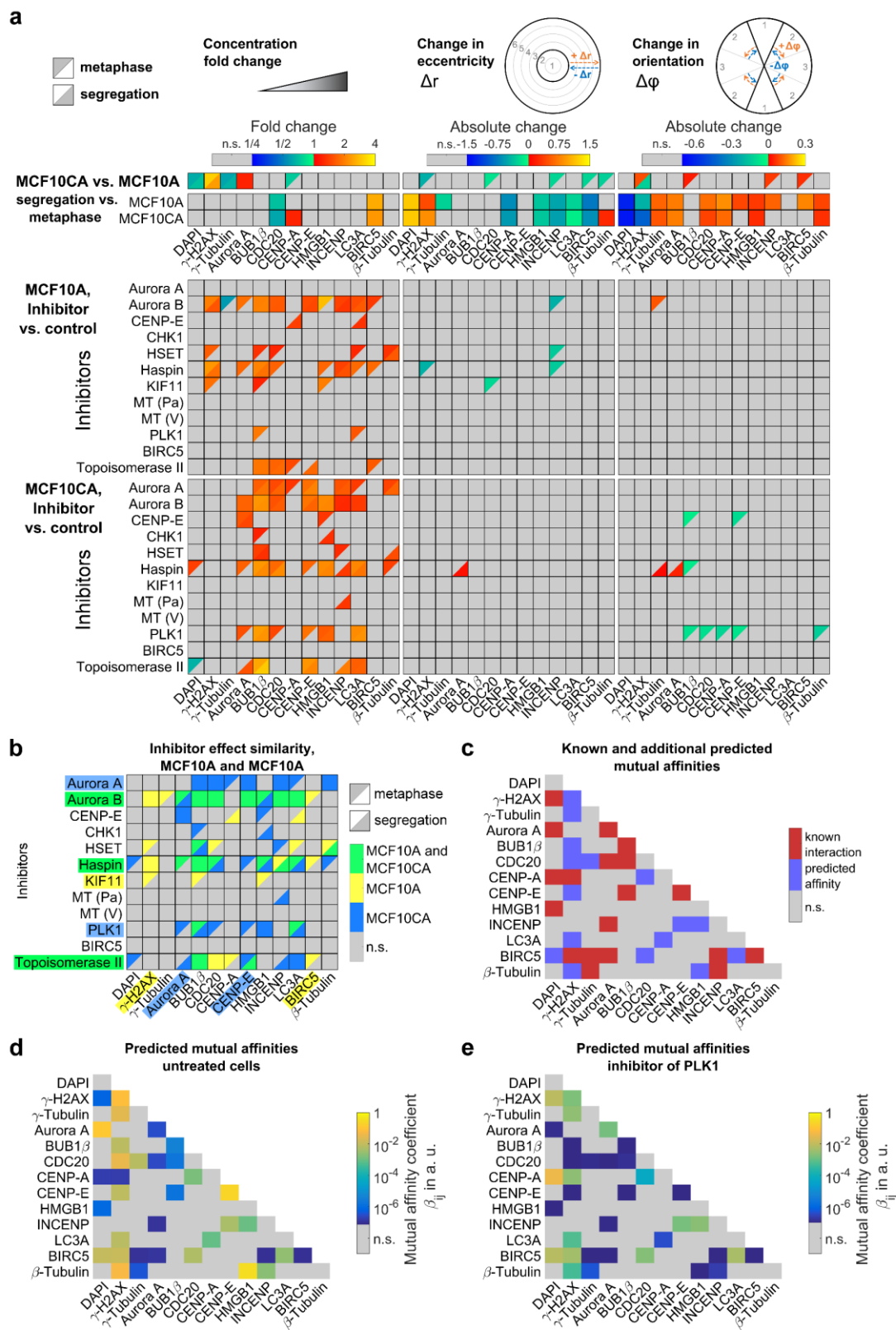


Figure 3 Inhibitor effects and estimates of affinities between proteins. (a) Concentration fold changes and localization changes, quantified as changes in eccentricity and orientation of localization patterns for comparisons between cell lines (MCF10CA vs. MCF10A), mitotic phases (segregation vs. metaphase) and inhibitor treatments (inhibitor vs. control). The left column shows color-coded fold changes in average concentrations (total intensities normalized by cell volumes) for DAPI and antibody stainings on a logarithmic scale. In the center column, eccentricity changes for intensity distributions in subcellular

compartments were visualized. Positive values describe a movement to the periphery while negative values represent a movement to the center of the cell. Similarly, in the right column, changes in angular orientation of intensity distributions were visualized. Positive values describe a movement towards the plane perpendicular to the cell division axis while negative values describe a movement towards the cell division axis. In cases of significant differences to negative controls (t-test with $p < 0.05$, followed by Bonferroni multiple testing correction for 54 comparisons in each column), fold changes relative to negative controls are indicated by colors (n. s., not significant). Values indicated separately for metaphase (upper left triangles) and segregation (lower right triangles) in (a) and (b). (b) Overlay of significant effects in MCF10A and MCF10CA cells, MCF10A only, or MCF10CA cells only. Color highlighted proteins denote predominant effects per row or column. (c) Known protein-protein interactions from Ingenuity Pathway Analysis overlaid with additional predicted mutual affinities between measured proteins (see **Supplementary Note 1**). For affinities to subcellular compartments, see **Supplementary Fig. 1** (d) Estimates of mutual affinities between measured proteins for untreated cells. (e) Estimated mutual affinities between measured proteins after treatment with an inhibitor of PLK1.

We next inspected changes in mutual affinities between mitotic proteins and their affinities to subcellular compartments upon drug treatment. To this end, the model with known and additionally predicted interactions was fitted to datasets from cells treated with inhibitors to estimate mutual affinities between proteins and to subcellular compartments. In **Fig. 3e**, estimated affinity coefficients for PLK1 as an exemplary inhibitor are visualized. Inhibition of PLK1 affected the localization patterns of several proteins and caused a strong specific shift in mutual affinities among several studied proteins in comparison to untreated cells (**Fig. 3d,e**). In those cases, many estimates of mutual affinities decreased, indicated by changes to blue color code. Contrarily, affinities to subcellular compartments during metaphase and segregation showed almost no differences to untreated cells (**Supplementary Fig. 1e-h**). It is tempting to speculate that effects of PLK1 inhibition are mediated through its involvement in spindle network formation²⁹. Specifically, predicted affinity of β -Tubulin to γ -H2AX, HMGB1 and INCENP decreased, and chromosome affinity of BIRC5 appears to be reduced by inhibition of PLK1, whereas the predicted affinity of INCENP to HMGB1 is increased (**Fig. 3e**). Reduced chromosome affinity of BIRC5 after PLK1 inhibition is in accordance with the finding that phosphorylation of BIRC5 by PLK1 is required for a proper chromosome alignment during mitosis¹².

To summarize, we present **3D SPECS**, a high-content screening assay employing automated iterative antibody labeling in 3D cell cultures. It allowed us to compare system-wide interactions between twelve proteins of two cell

lines in two mitotic phases, upon twelve individual treatments. High automation comprises detection of mitoses, iterative staining and imaging, 3D partitioning, modeling and visualization using **SpheriCell**, a novel approach that does not require antibody image segmentation, nor alignment of cell division in 3D. This explorative approach recapitulated *prior* knowledge on proteins involved in mitosis and allowed the generation of novel hypotheses in mitotic pathway signaling. Most prominently, we discovered up-regulation of γ -H2AX in tumorigenic MCF10CA cells compared to MCF10A. Further, γ -H2AX has a higher sensitivity to interference in MCF10A, which in turn appears to have a more robust spindle apparatus. Our novel combined imaging and mathematical modeling approach allowed us to disentangle inhibitor-mediated protein localization and binding affinity changes and showed that changes in affinities between proteins (**Fig. 3d,e**) were more pronounced than changes in individual protein localizations (**Supplementary Fig. 2d,e**). As an example, we focused on the measured inhibitions of PLK1 activity, which is responsible for establishing the mitotic spindle and which is frequently hyper-activated in cancer³⁰. Subsequent reduction in chromatin affinity of BIRC5 could be explained by its dependency on PLK1 phosphorylation¹², most likely intertwined with CPC function.

Our method can be readily extended to directly determine the activity of proteins by phospho-specific antibodies. For a more fine-grained assessment of protein localization additional nuclear or membrane staining can be easily integrated into **3D SPECS**. The **SpheriCell** approach that renders intuitively simple and comprehensive visualization of protein localization in cell division can also be amended by including polar landmarks of non-dividing cells. Taken together we have demonstrated **3D SPECS** as a novel workflow unraveling thus unprecedented levels of details in changes of protein localization and interaction upon drug treatment of three-dimensional cell cultures.

Acknowledgements

We thank Sabine Aschenbrenner for support with lab techniques, Siegfried Winkler, Leo Burger, and Helmuth Schaar for microscopy hardware, Antonio Politi for imaging advice and ZEN black macro interface, Maria Maier for assistance with 3D renderings, Christian Dietz for continued development of KNIME image processing, and Clarissa Liesche and Joël Beaudoin for critical comments. The authors acknowledge support by the state of Baden-Württemberg through bwHPC.

Author contributions

L.M. and C.C. conceived the experiments and subcellular visualization strategy. L.M., K.J. and M.W. established antibody staining and drug treatment protocols. L.M. developed automated iterative staining workflow, conducted experiments, and image analysis. S.K. developed the interaction model and performed statistical tests. C.C. and R.E. supervised this project. L.M., S.K., C.C. and R.E. wrote the manuscript. All authors commented on the manuscript.

Competing financial interests

The authors declare no competing financial interests.

References

1. Gerdes, M. J. *et al.* Highly multiplexed single-cell analysis of formalin-fixed, paraffin-embedded cancer tissue. *Proc. Natl. Acad. Sci. U. S. A.* **110**, 11982–7 (2013).
2. Cappella, P. & Gasparri, F. Highly Multiplexed Phenotypic Imaging for Cell Proliferation Studies. *J. Biomol. Screen.* **19**, 145–157 (2014).
3. Lin, J.-R. Multiplexed Single-Cell Imaging: Past, Present, and Future. *Assay Drug Dev. Technol.* **15**, 8–10 (2017).
4. Bodenmiller, B. Multiplexed Epitope-Based Tissue Imaging for Discovery and Healthcare Applications. *Cell Syst.* **2**, 225–238 (2016).
5. Horvath, P. *et al.* Screening out irrelevant cell-based models of disease. *Nat. Rev. Drug Discov.* **15**, 751–769 (2016).
6. Marques, S., Fonseca, J., Silva, P. & Bousbaa, H. Targeting the Spindle Assembly Checkpoint for Breast Cancer Treatment. *Curr. Cancer Drug Targets* **15**, 272–281 (2015).
7. Chan, K.-S., Koh, C.-G. & Li, H.-Y. Mitosis-targeted anti-cancer therapies: where they stand. *Cell Death Dis.* **3**, e411 (2012).
8. Otto, T. & Sicinski, P. Cell cycle proteins as promising targets in cancer therapy. *Nat. Rev. Cancer* **17**, 93–115 (2017).
9. Petersen, O. W., Rønnov-Jessen, L., Howlett, a R. & Bissell, M. J. Interaction with basement membrane serves to rapidly distinguish growth and differentiation pattern of normal and malignant human breast epithelial cells. *Proc. Natl. Acad. Sci. U. S. A.* **89**, 9064–8 (1992).
10. Maguire, S. L. *et al.* Three-dimensional modelling identifies novel genetic dependencies associated with breast cancer progression in the isogenic MCF10 model. *J. Pathol.* **240**, 315–328 (2016).
11. Debnath, J. & Brugge, J. S. Modelling glandular epithelial cancers in three-dimensional cultures. *Nat. Rev. Cancer* **5**, 675–688 (2005).
12. Carmena, M., Wheelock, M., Funabiki, H. & Earnshaw, W. C. The chromosomal passenger complex (CPC):

from easy rider to the godfather of mitosis. *Nat. Rev. Mol. Cell Biol.* **13**, 789–803 (2012).

13. London, N. & Biggins, S. Signalling dynamics in the spindle checkpoint response. *Nat. Rev. Mol. Cell Biol.* **15**, 736–47 (2014).
14. Carmena, M. & Earnshaw, W. C. The cellular geography of aurora kinases. *Nat. Rev. Mol. Cell Biol.* **4**, 842–854 (2003).
15. Musacchio, A. & Salmon, E. D. The spindle-assembly checkpoint in space and time. *Nat. Rev. Mol. Cell Biol.* **8**, 379–393 (2007).
16. Paull, T. T. *et al.* A critical role for histone H2AX in recruitment of repair factors to nuclear foci after DNA damage. *Curr. Biol.* **10**, 886–895 (2000).
17. Pallier, C. *et al.* Association of chromatin proteins high mobility group box (HMGB) 1 and HMGB2 with mitotic chromosomes. *Mol. Biol. Cell* **14**, 3414–26 (2003).
18. Mariño, G., Niso-Santano, M., Baehrecke, E. H. & Kroemer, G. Self-consumption: the interplay of autophagy and apoptosis. *Nat. Rev. Mol. Cell Biol.* **15**, 81–94 (2014).
19. Jordan, M. A. & Wilson, L. Microtubules as a target for anticancer drugs. *Nat. Rev. Cancer* **4**, 253–65 (2004).
20. Moritz, M., Braunfeld, M. B., Sedat, J. W., Alberts, B. & Agard, D. A. Microtubule nucleation by γ -tubulin-containing rings in the centrosome. *Nature* **378**, 638–640 (1995).
21. Petsalaki, E. & Zachos, G. Clks 1, 2 and 4 prevent chromatin breakage by regulating the Aurora B-dependent abscission checkpoint. *Nat. Commun.* **7**, 11451 (2016).
22. D’Assoro, A. B. *et al.* The mitotic kinase Aurora-A promotes distant metastases by inducing epithelial-to-mesenchymal transition in ER α + breast cancer cells. *Oncogene* **33**, 599–610 (2014).
23. Sullivan, M. & Morgan, D. O. Finishing mitosis, one step at a time. *Nat. Rev. Mol. Cell Biol.* **8**, 894–903 (2007).
24. Nitiss, J. L. DNA topoisomerase II and its growing repertoire of biological functions. *Nat. Rev. Cancer* **9**, 327–337 (2009).
25. Rath, O. & Kozielski, F. Kinesins and cancer. *Nat. Rev. Cancer* **12**, 527–539 (2012).

26. Müller, H., Fogeron, M.-L., Lehmann, V., Lehrach, H. & Lange, B. M. H. A centrosome-independent role for gamma-TuRC proteins in the spindle assembly checkpoint. *Science* **314**, 654–7 (2006).
27. Nitiss, J. L. Targeting DNA topoisomerase II in cancer chemotherapy. *Nat. Rev. Cancer* **9**, 338–350 (2009).
28. Chan, G. K., Schaar, B. T. & Yen, T. J. Characterization of the kinetochore binding domain of CENP-E reveals interactions with the kinetochore proteins CENP-F and hBUBR1. *J. Cell Biol.* **143**, 49–63 (1998).
29. Zitouni, S., Nabais, C., Jana, S. C., Guerrero, A. & Bettencourt-Dias, M. Polo-like kinases: structural variations lead to multiple functions. *Nat. Rev. Mol. Cell Biol.* **15**, 433–452 (2014).
30. Kumar, S., Sharma, G., Chakraborty, C., Sharma, A. R. & Kim, J. Regulatory functional territory of PLK-1 and their substrates beyond mitosis. *Oncotarget* **8**, 37942–37962 (2017).
31. Lin, J.-R., Fallahi-Sichani, M. & Sorger, P. K. K. Highly multiplexed imaging of single cells using a high-throughput cyclic immunofluorescence method. *Nat. Commun.* **6**, 8390 (2015).
32. Debnath, J., Muthuswamy, S. K. & Brugge, J. S. Morphogenesis and oncogenesis of MCF-10A mammary epithelial acini grown in three-dimensional basement membrane cultures. *Methods* **30**, 256–268 (2003).
33. Muthuswamy, S. K., Li, D., Lelievre, S., Bissell, M. J. & Brugge, J. S. ErbB2, but not ErbB1, reinitiates proliferation and induces luminal repopulation in epithelial acini. *Nat. Cell Biol.* **3**, 785–792 (2001).
34. Gerdes, M. J. *et al.* Sequential analysis of biological samples. *US Patent 7,741,045*, (2010).
35. Berthold, M. R. *et al.* in *Data Analysis, Machine Learning and Applications SE - 38* (eds. Preisach, C., Burkhardt, H., Schmidt-Thieme, L. & Decker, R.) 319–326 (Springer Berlin Heidelberg, 2008). doi:10/cwm8p3
36. Schindelin, J. *et al.* Fiji: an open-source platform for biological-image analysis. *Nat. Methods* **9**, 676–682 (2012).
37. Parslow, A., Cardona, A. & Bryson-Richardson, R. J. Sample Drift Correction Following 4D Confocal Time-lapse Imaging. *J. Vis. Exp.* e51086 (2014). doi:10.3791/51086
38. Thevenaz, P., Ruttimann, U. E. & Unser, M. A pyramid approach to subpixel registration based on intensity. *IEEE Trans. Image Process.* **7**, 27–41 (1998).

39. Leopardi, P. A partition of the unit sphere into regions of equal area and small diameter. *Electron. Trans. Numer. Anal.* **25**, 309–327 (2006).
40. Ollion, J., Cochenec, J., Loll, F., Escude, C. & Boudier, T. TANGO: a generic tool for high-throughput 3D image analysis for studying nuclear organization. *Bioinformatics* **29**, 1840–1841 (2013).
41. Wickham, H. *ggplot2: Elegant Graphics for Data Analysis*. (Springer, 2009).
42. Pau, G., Fuchs, F., Sklyar, O., Boutros, M. & Huber, W. EBIImage---an R package for image processing with applications to cellular phenotypes. *Bioinformatics* **26**, 979–981 (2010).

Online Methods

Mitotic proteins were assessed after 48h drug treatment by iterative immunofluorescence labeling. The antibodies were either labeled with one of DyLight 550 / Cy3 or DyLight 650 / Cy5. Both types of dyes could be used interchangeably in terms of excitation and emission spectra.

While Matrigel is essential for acinar growth of spheroids¹¹, it also dissolves quickly when the bleaching solution is applied. Therefore, we have used DyLight instead of Cy or Alexa³¹ labeled antibodies, as they bleach much faster and have a very strong fluorescence signal nevertheless. Applying the bleaching solution significantly longer than 5 minutes at a time typically dissolved the Matrigel carrying the spheroids.

All treatments were imaged at 30 spheroids that showed at least one mitosis each. 196 stacks per well, eight wells per round and four rounds resulted in 6272 image stacks with 21 slices each that were automatically pre-screened for mitotic events. Iterative high resolution images of 30 positions per well in eight wells in each of four rounds totaled in 960 identified spheroids that were imaged each with 31 slices, after staining and after bleaching in six iterations.

For analysis and visualization, every mitosis was aligned along its division plane for a spherical neighborhood that contains the cell division in equatorial axis (see Fig. 1b).

3D cell culture and drug treatment Human mammary epithelial MCF10A pBabePuro cells were kindly obtained from Zev Gartner Lab; MCF10CA1d.cl1 (MCF10CA) cells from Karmanos Cancer Institute. Eight well Lab-Tek Chambered Coverglass slides (Sigma 155411) were treated with 2 M NaOH for 20 min and rinsed twice for 10 min with MilliQ water. Ten μ l Matrigel (growth factor reduced, phenol red-free, Corning 356231) per well was added on ice with pipette tips pre-cooled to -20 °C. MCF10A and CA cells were seeded with 2% Matrigel in Growth Medium overnight. Growth medium was adapted from Debnath et al.³² and is based on DMEM/F12 (no phenol red, Gibco 21041-33), with 5% Horse Serum (Gibco 16050-122), 20 ng/ml EGF (Sigma E9644-.2MG), 0.5 mg/ml Hydrocortisone (Sigma H0888-1g), 100 ng/ml Cholera Toxin (Sigma C8052-1MG), 10 μ g/ml Insulin (Life Technologies 12585014). For the inhibition experiments, the cells were treated for 48h at one day after seeding.

Inhibitors Drugs, suppliers, and concentrations used were Barasertib (Aurora B inhibitor; alternative name AZD1152-HQPS; SelleckChem S1147; 1.11 nM); CHR-6494 (Haspin inhibitor; MedChem Express HY-15217; 500 nM); CW069 (HSET inhibitor; SelleckChem S7336; 25.0 μ M); Etoposide (Topoisomerase II inhibitor; SelleckChem S1225; 333 nM); GSK461364 (PLK1 inhibitor; SelleckChem S2193; 2.20 nM); GSK923295 (CENP-E inhibitor; SelleckChem S7090; 3.20 nM); Ispinesib (KIF11 inhibitor; alternative name SB-715992; SelleckChem S1452; 1.70 nM); MK-5108 (Aurora A inhibitor; alternative name VX-689; SelleckChem S2770; 0.576 nM); MK-8776 (CHK1 inhibitor; alternative name SCH 900776; SelleckChem S2735; 9.00 nM); Paclitaxel (microtubule inhibitor; SelleckChem S1150; 2.67 nM); Vinblastine (microtubule inhibitor; Sigma V1377; 2.40 nM); and YM155 (BIRC5 inhibitor; SelleckChem S1130; 0.540 nM).

Antibodies and labeling kits Antibodies were conjugated with DyLight 550 and 650 Microscale labeling kits per supplier reference manual (Sigma, 84531 and 84536, respectively) unless otherwise stated. Antibody targets, dilutions, supplier, and conjugation method in iterative staining order were CENP-E (1:400; Abnova MAB1924; conjugated DyLight 550); BubR1 (1:600; Thermo Fisher MA5-16036; pre-conjugated with DyLight 650); beta-Tubulin (1:5000; Abcam ab11309; pre-conjugated with Cy3); CDC20 (1:400; Bethyl A301-179A; conjugated DyLight 550); gamma-Tubulin (1:12000; Abcam ab176404; pre-conjugated with Cy3); LC3A, microtubule-associated proteins 1A/1B light chain 3A (1:400; Novus NB100-2331; conjugated DyLight 650); BIRC5 (1:1000; Abcam ab176402; pre-conjugated with Cy3) INCENP (1:1000; Thermo Fisher MA5-17100; conjugated DyLight 650); Aurora A (1:6000; Abcam ab176375; pre-conjugated with Cy3); CENP-A (1:500; Abnova PAB18324; conjugated DyLight 650); HMGB1 (1:3000; Abcam ab176398; pre-conjugated with Cy3); H2AX (1:2500; Cell Signaling 9718BF; conjugated DyLight 650).

Iterative antibody labeling Cell fixation was based on a protocol from Debnath et al.³², with 1.85% formaldehyde solution (Sigma 252549) added to the medium for 10 minutes. Cells were rinsed twice with PBS and permeabilized for 10 min at RT with 0.5% TX-100 pre-chilled to 8 °C, washed three times with PBS-glycine (130 mM NaCl, 7 mM Na₂HPO₄, 3.5 mM NaH₂PO₄, 100 mM glycine) for 10 minutes, and blocked overnight at RT in a blocking solution consisting of IF-wash solution³³ (130 mM NaCl, 7 mM Na₂HPO₄, 3.5 mM NaH₂PO₄, 7.7 mM NaN₃, 0.1% BSA, 0.2% Triton X-100, 0.05% Tween 20) with 10% goat serum (Sigma G9023-10ML) and 1:1000 DAPI (Sigma D8417-1MG), inside an opaque EMBL microscope incubation chamber. For each iteration, two antibodies were diluted in freshly prepared blocking solution and stored in a slide within a 4x LabTek holder (EMBLEM LTT-01 and LTT-02). They were

automatically pipetted into the wells by a peristaltic pump of the ProCellcare 5030 system (ProDesign) and incubated for 3h, washed twice with IF-wash for 5 min and three times with PBS for 5 min. After imaging, freshly prepared H₂O₂ bleaching solution³⁴ containing 3% H₂O₂ (AppliChem, Cat. No. 121076) and 0.1M Na₂CO₃/NaHCO₃ buffer at pH \approx 10 was stored in another LabTek. It was automatically applied for 5 minutes and washed twice with PBS for 5 minutes. Standard incubator light source was switched on during bleaching with Energenie EG-PM2. Pipetting positions were planned with Zeiss Zen blue (www.zeiss.com/zen) and pipetting workflow was implemented in LabView (www.ni.com/labview).

Pre-screen During blocking, slides were imaged with a Yokogawa CSU-X1 spinning disc unit attached to a Zeiss Observer Z1 inside an EMBL incubation chamber. 196 image stacks of 401.6 x 400 x 60 μ m were taken per well with a plan-apochromat 20x/0.8 NA objective. Stack slices had 1004x1002 pixels, step size was 3 μ m and exposure 40 ms. Candidate mitotic positions were detected via their DAPI signal by a custom KNIME workflow and selected or expanded manually if necessary. The automatic selection excludes monolayer slices and uses a supervised tree ensemble classifier (comparable to a random forest). For each treatment and cell line, 30 positions of spheroids with at least one mitosis each were selected for imaging during the iterative staining workflow.

Acquisition of iterative staining images After each round of bleaching or staining, spheroids were automatically imaged with a laser scanning confocal Zeiss LSM 780 connected to the same Axio Observer as the spinning disc unit. Stack dimensions were 106.07 x 106.07 x 60 μ m, with 512 x 512 pixels per slice and 2 μ m Z steps. Objective was plan-apochromat 20x/0.8 NA, pixel dwell time 3.15 μ s, and pinhole 32 μ m. Emission spectra were taken at 410 – 489 nm (DAPI), 560 – 586, 586 – 612, and 612 – 630 (three parts of Cy3 / DyLight 550), and 638 – 758 nm (Cy5 / DyLight 650).

Image processing Splitting the emission spectrum from 560 to 630 nm in three parts allowed for post-acquisition exposure correction. Only for BIRC5 it was necessary to exclude the strongest emission channel from the labeling image. All remaining split channels were averaged. Mitotic DAPI signal was segmented in 3D by a customized region growing algorithm³⁵ with manual seeds and borders to closely neighboring nuclei, especially in Z-direction.

Segmented areas were manually annotated with their mitotic phase and ana- / telophases joined. Assignment of segregating split chromatin regions to a single dividing cell was verified with β -Tubulin staining. Registration of consecutive stacks per imaging position used subpixel alignment of Fiji³⁶ plugin Correct 3D Drift³⁷ followed by MultiStackReg³⁸ with scaled rotation. Registration of the stacks was verified manually. For the spherical neighborhood, images were interpolated linearly in Z to match the X/Y pixel dimensions. Spherical segment angles were generated by Recursive Zonal Equal Area Sphere Partitioning Toolbox³⁹ in MATLAB (www.mathworks.com) for 180 areas. A custom R script was created to join the areas to segments and to fit them in size and orientation to the individual mitoses, which were identified with 3D ellipsoid fit of the 3D ImageJ suite⁴⁰. Metaphases could use those values as-is, but the size of segregating cells was overestimated by the ellipsoid fit and replaced by the centroid distances of their individual chromatin regions. Their 3D orientation used the average of the first two eigenvectors and the normalized centroid to centroid vector as third. The six spherical neighborhood shells grow linearly in their radius from the mitotic center, and the inner four span the identified nucleus area. Missing cells due to loss of Matrigel or failed registration were removed from further analysis. All image processing steps were embedded in a KNIME³⁵ workflow.

Visualization Antibody intensities are depicted as color-coded mean values for three distinct segment classes (phi levels, **Fig. 1b**). Decreased intensity dependent on imaging depth was corrected by the mean DAPI intensity within the individual spherical neighborhood and mean DAPI intensity per well in pre-screen images after z-projection. To avoid an artificial increase in background signal of antibodies, DAPI intensities below a minimum threshold were excluded. Highlighting of partitions was determined by the control intensity over all rounds. Data was visualized with the packages ggplot2⁴¹, EBImage⁴², and shiny (shiny.rstudio.com) for R (www.r-project.org).

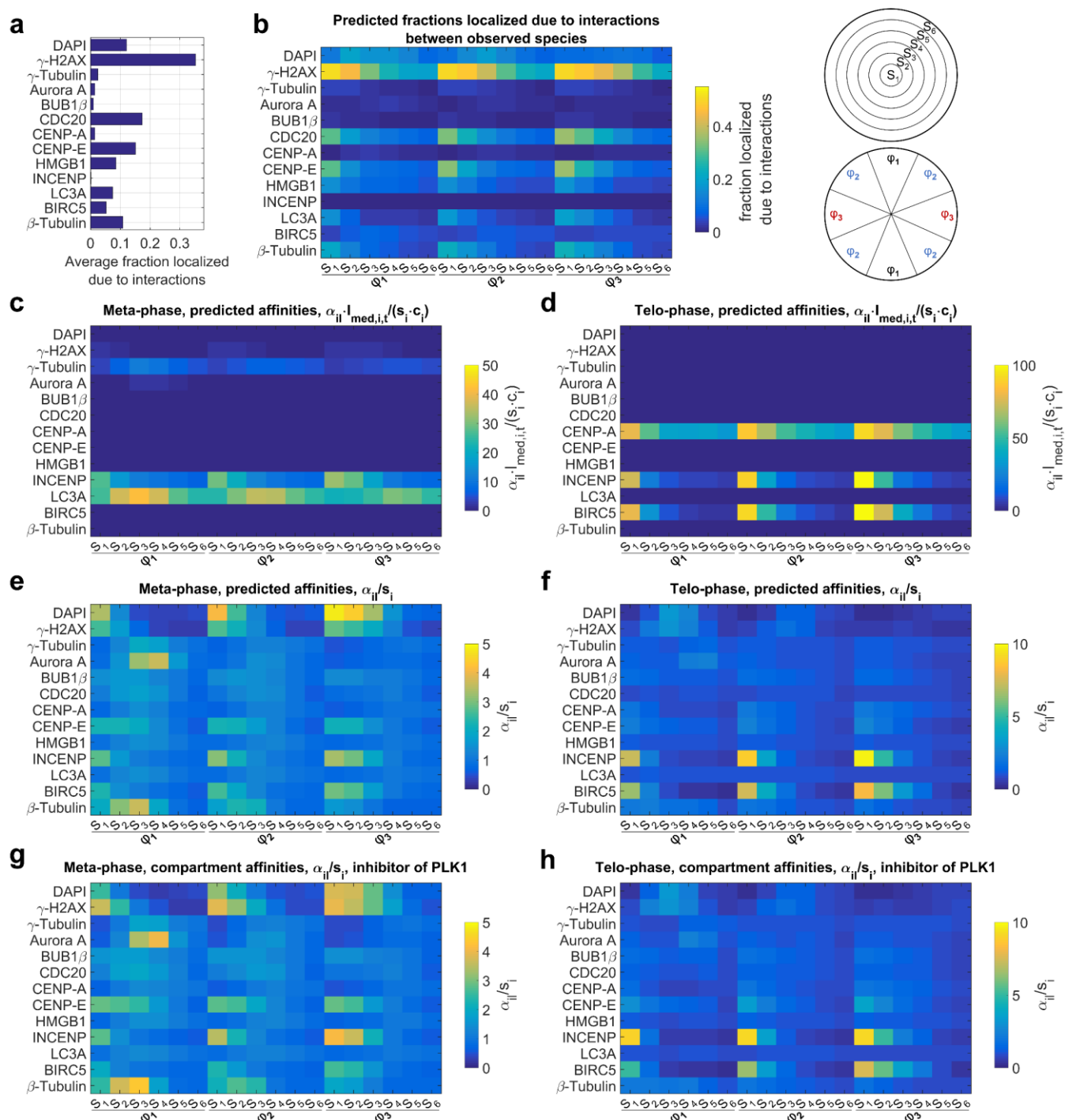
Statistics and mathematical modeling To test for significance of comparisons between controls and inhibitor treatments, we applied two-sample t-tests. For comparisons between two groups, intensity values for all subcellular compartments were collected within each group. In total, 54 comparisons were made between measurements of each protein. Therefore, t-tests with $p < 0.05/54$ were regarded as significant (Bonferroni correction for multiple testing). The interaction model was implemented in MATLAB. For model calibration, we applied the solver lsqnonlin

using the trust-region-reflective algorithm. Details on the model formulation and fitting can be found in **Supplementary Note 1**.

Interpretation Known interactions from literature were generated through the use of QIAGEN's Ingenuity® Pathway Analysis (IPA®, QIAGEN Redwood City, www.qiagen.com/ingenuity). They are supported by at least one reference from the literature, from a textbook, or from canonical information stored in the Ingenuity Pathways Knowledge Base.

Data and code availability Spherical neighborhoods, their image sources, and custom software code is available upon request.

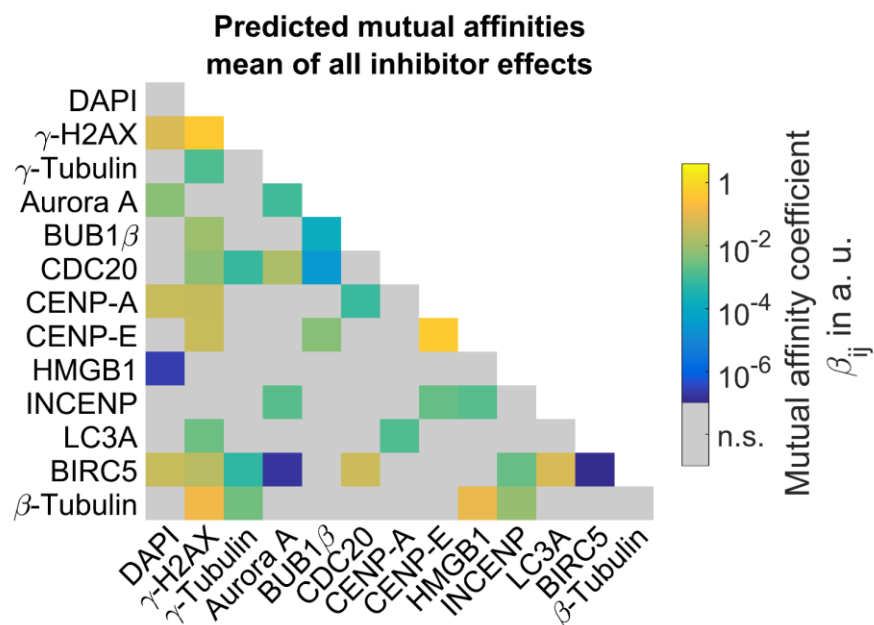
Supplementary Material



Supplementary Figure 1 Predicted localization affinities. (a) Predicted fractions of proteins recruited to subcellular compartments due to mutual affinities between proteins. (b) Predicted fractions of proteins recruited due to mutual affinities between proteins, distinguished by eccentricity intervals (S_1 to S_6) and orientations (ϕ_1 to ϕ_6) as indicated by schematic maps. (c) Affinity estimates $\tilde{\alpha}_{il} = \alpha_{il} I_{med, i, t} / (s_i c_i)$, before dividing by scaling factor estimates, during metaphase or segregation obtained by model fitting to dataset from untreated cells (see **Supplementary Note 1** for

details). (d) Rescaled untreated localization affinities α_{il}/s_i during metaphase or segregation. (e) Rescaled

localization affinities α_{il}/s_i upon treatment with PLK1.



Supplementary Figure 2 Average mutual affinities of all inhibitor effects.

a

Antibody	Alternative Name	Fluorophore
Aurora kinase A	Aurora A	Cy3
Bub1 β	BubR1	DyLight 650
CDC20		DyLight 650
CENP-A		DyLight 650
CENP-E		DyLight 550
H2AX		DyLight 550
HMGB1		Cy3
INCENP		DyLight 650
MAP1LC3A	LC3	DyLight 650
BIRC5	Survivin	Cy3
β -Tubulin		Cy3
γ -Tubulin		DyLight 550

b

Target	Alternative Name	Drug
Aurora kinase A	Aurora A	MK-5108
Aurora kinase B	Aurora B	Barasertib
CENP-E		GSK923295
Chk1		MK-8776
Haspin		CHR-6494
KIFC1	HSET	CW069
Kif11	Eg5	Ispinesib
Microtubules		Paclitaxel
Microtubules		Vinblastine
PLK1		GSK461364
BIRC5	Survivin	YM155
Topoisomerase II		Etoposide

c

Cell Line	Type
MCF10A	non-tumorigenic
MCF10CA	Tumorigenic

Supplementary Table 1 Assay proteins. (a) Antibodies and fluorophores. (b) Inhibitors and their targets. (c) Cell lines and their type.

Supplementary Note 1

Calculation of the center of eccentricity and center of orientation measures

We compared DAPI and antibody staining intensities between cell lines, mitotic phases and for inhibitor treatments relative to controls. To this end, fluorescence intensity values were normalized by mitotic bin volumes to obtain intensity measures that were proportional to concentrations. To compare spatial distributions of protein intensities between cell lines, mitotic phases and inhibitor treatments, we defined characteristic measures of eccentricity and orientation. For each cell, 18 ROIs were defined as intersections between six eccentricity shells with indices $\mu=1\dots6$ and three orientations relative to the division plane (equatorial, $[-30^\circ;30^\circ]$; diagonal, $[30^\circ,60^\circ]$; polar, $[60^\circ,120^\circ]$) with indices $\nu=1\dots3$. The center of eccentricity r was defined by a sum of eccentricities r_μ weighted by fluorescence intensities $I_{\mu\nu}$

$$r = \frac{\sum_{\mu=1}^6 \sum_{\nu=1}^3 I_{\mu\nu} r_\mu}{I_c} \quad (1)$$

with the total sum of intensities $I_c = \sum_{\mu=1}^6 \sum_{\nu=1}^3 I_{\mu\nu}$. Similarly, the center of orientation φ was defined by

$$\varphi = \frac{\sum_{\mu=1}^6 \sum_{\nu=1}^3 I_{\mu\nu} \varphi_\nu}{I_c}. \quad (2)$$

In the middle and right column of **Fig. 3a**, significant changes of r and φ dependent on cell lines, mitosis phases and inhibitor treatments were visualized. To test for significance, we performed two-sample t-tests. Given the assumption that intensity measures are in general normally distributed, this is valid for weighted sums of intensities. From applying (Bonferroni) correction for multiple testing for a total of 54 comparisons based on measurements for each protein, significance was defined by $p < 0.05/54 \approx 9.26 \cdot 10^{-4}$.

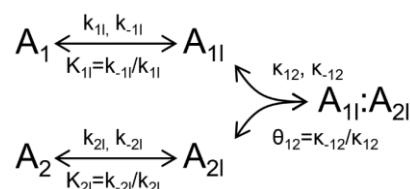
Mathematical model of protein affinities to subcellular compartments and mutual affinities between proteins

To describe binding of proteins to subcellular compartments and mutual binding of proteins within subcellular compartments, we constructed a mathematical model derived from ordinary differential equations (ODEs). Here, we describe the concept and the implementation of this model.

In the simplest case, we consider binding of two proteins A_1 and A_2 . Concentrations of free species are denoted by A_1 and A_2 (**Supplementary Note Figure 1**). Binding to mitotic bin l , results in A_{1l} and A_{2l} with concentrations A_{1l} and A_{2l} . Kinetic parameters describing A_1 binding and unbinding to this compartment are k_{1l} and k_{-1l} , while A_2 binding and unbinding is described by k_{2l} and k_{-2l} . We assume that binding sites for proteins in a compartment are not limiting. The equation describing the concentration of free A_1 thus reads

$$\frac{dA_1}{dt} = -k_{1l}A_1 + k_{-1l}A_{1l}. \quad (3)$$

Dissociation constants $K_{1l} = k_{-1l}/k_{1l}$ and $K_{2l} = k_{-2l}/k_{2l}$ are thus dimensionless parameters. In steady state, the concentrations for A_1 and A_2 bound to mitotic bin l equal $A_{1l} = A_1/K_{1l}$ and $A_{2l} = A_2/K_{2l}$.



Supplementary Note Figure 1 Binding of species A_1 and A_2 to mitotic bin l results in A_{1l} and A_{2l} . Mutual binding in this compartment results in $A_{1l}:A_{2l}$.

In mitotic bin l , A_{1l} can reversibly bind to A_{2l} , resulting in $A_{1l}:A_{2l}$ with concentration $A_{1l}:A_{2l}$. We assume that binding between A_{1l} and A_{2l} depends only on the interaction between the proteins but not on the mitotic bin. Their binding and unbinding is described by parameters κ_{12} and κ_{-12} , and the dissociation constant $\theta_{12} = \kappa_{-12}/\kappa_{12}$. ODEs for A_{1l} and $A_{1l}:A_{2l}$ read

$$\frac{dA_{1l}}{dt} = k_{1l}A_1 - k_{-1l}A_{1l} - \kappa_{12}A_{1l}A_{2l} + \kappa_{-12}A_{1l} : A_{2l} \quad (4)$$

$$\frac{dA_{1l} : A_{2l}}{dt} = \kappa_{12}A_{1l}A_{2l} - \kappa_{-12}A_{1l} : A_{2l}. \quad (5)$$

Solving at steady state for the concentration of $A_{1l} : A_{2l}$ results in

$$A_{1l} : A_{2l} = \frac{A_1A_2}{K_{1l}K_{2l}\theta_{12}}. \quad (6)$$

After immunofluorescence staining for A_1 , the fluorescence intensity in mitotic bin l is therefore given by

$$I_{1l} = c_1(A_{1l} + A_{1l} : A_{2l}) = c_1\left(\frac{A_1}{K_{1l}} + \frac{A_1A_2}{K_{1l}K_{2l}\theta_{12}}\right). \quad (7)$$

In this equation, the scaling factor c_1 relates concentrations to fluorescence intensity values. The measured intensity thus depends linearly on the concentration of A_1 and further contains the product of concentrations A_1 and A_2 . This resembles that A_1 and A_2 are either recruited to mitotic bin l due to their affinity to this compartment or due to their mutual affinity.

To generalize this model, we describe binding of proteins A_i with $i = 1..n$ to subcellular compartments $l = 1..m$. Affinities of proteins A_i to a mitotic bin are described by the n-by-m matrix $\alpha_{il} = 1/K_{il}$, whereas affinities between proteins are given by the n-by-n matrix $\beta_{ij} = 1/\theta_{ij}$. Then, intensities of all species in all subcellular compartments of a cell are given by

$$I_{il} = c_i\left(\frac{A_i}{K_{il}} + \sum_{j=1}^n \frac{A_iA_j}{K_{il}K_{jl}\theta_{ij}}\right) = c_i\left(\alpha_{il}A_i + \sum_{j=1}^n \alpha_{il}\alpha_{jl}\beta_{ij}A_iA_j\right). \quad (8)$$

For parameter estimations, we made the simplifying assumption that the concentrations of free proteins A_i were approximately proportional to the average cellular concentrations $A_{i,t} = s_iA_i$, with the proportionality factor $s_i \geq 1$. This assumption holds true if the proteins are recruited to subcellular compartments due to their direct affinities to mitotic compartments rather than their affinities to the other observed proteins, which will be justified below.

Average cellular intensities were calculated by weighting intensities in subcellular compartments I_{il} with mitotic bin

volumes V_l , given by

$$I_{i,t} = \frac{\sum_{l=1}^m I_{il} V_l}{\sum_{l=1}^m V_l}. \quad (9)$$

For model fitting, we calculated fold changes relative to medians of average concentrations for the population of cells, $\hat{I}_{i,t}$, for intensities in subcellular compartments, $\tilde{I}_{il} = I_{il} / \hat{I}_{i,t}$, and for average cellular concentrations,

$\tilde{I}_{i,t} = I_{i,t} / \hat{I}_{i,t}$. Then, experimental measurements could be related to model variables A_i by

$$\tilde{I}_{i,t} = \frac{I_{i,t}}{\hat{I}_{i,t}} = \frac{s_i c_i}{\hat{I}_{i,t}} A_i. \quad (10)$$

Thereby, Eq. 8 was rescaled to

$$\tilde{I}_{il} = \frac{c_i}{\hat{I}_{i,t}} \left(\frac{\alpha_{il} \hat{I}_{i,t}}{s_i c_i} \tilde{I}_{i,t} + \sum_{j=1}^n \frac{\alpha_{il} \hat{I}_{i,t}}{s_i c_i} \frac{\alpha_{jl} \hat{I}_{j,t}}{s_j c_j} \beta_{ij} \tilde{I}_{i,t} \tilde{I}_{j,t} \right) \equiv d_i \tilde{\alpha}_{il} \tilde{I}_{i,t} \left(1 + \sum_{j=1}^n \tilde{\alpha}_{jl} \beta_{ij} \tilde{I}_{j,t} \right). \quad (11)$$

Therein, the rescaled parameter $d_i = c_i / \hat{I}_{i,t}$ was equal to the inverse of the median average cellular concentration,

and $\tilde{\alpha}_{il} = \frac{\alpha_{il} \hat{I}_{i,t}}{s_i c_i}$ was equal to the median concentration of species A_i that was bound in mitotic bin l .

To account for different affinities of proteins to subcellular compartments during metaphase and segregation,

$\tilde{\alpha}_{meta,il}$ and $\tilde{\alpha}_{segr,il}$, as well as scaling factors $d_{meta,i}$ and $d_{segr,i}$, intensity measurements during these cell cycle phases were separately described by

$$\tilde{I}_{meta,il} = d_{meta,i} \tilde{\alpha}_{meta,il} \tilde{I}_{meta,i,t} \left(1 + \sum_{j=1}^n \tilde{\alpha}_{meta,jl} \beta_{ij} \tilde{I}_{meta,j,t} \right) \quad (12)$$

and

$$\tilde{I}_{segr,il} = d_{segr,i} \tilde{\alpha}_{segr,il} \tilde{I}_{segr,i,t} \left(1 + \sum_{j=1}^n \tilde{\alpha}_{segr,jl} \beta_{ij} \tilde{I}_{segr,j,t} \right). \quad (13)$$

Thereby, we assume that rescaled affinities to subcellular compartments, but not mutual affinities between proteins β_{ij} , were dependent on the cell cycle phase. We simultaneously fitted Eqs. (12) and (13) to experimental data for estimating $d_{meta,i}$, $d_{segr,i}$, $\tilde{\alpha}_{meta,il}$, $\tilde{\alpha}_{segr,il}$ and β_{ij} .

To analyze relevant interactions between proteins, we first used experimental data from controls (cells not treated with inhibitors). Data from MCF10A and MCF10CA cells were fitted together, assuming that differences between cell lines were only dependent on different average cellular concentrations of all proteins but not on affinities to subcellular compartments or affinities between proteins. A total of 513 to 529 parameters were estimated by model fitting to 50.635 data points (47.970 intensity measurements for subcellular compartments and 2665 average intensity values) from control experiments in 205 cells. To equally weight residuals for data points of different magnitudes we assumed the error model

$$\varepsilon(\tilde{I}_{il}) = 0.05 \cdot \tilde{I}_{il} + 0.05 \cdot \max(\tilde{I}_{il}), \quad (14)$$

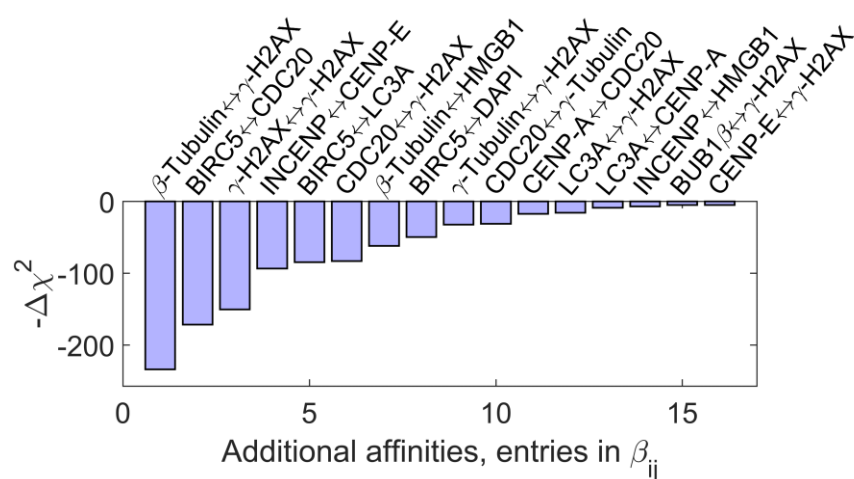
assuming that for each measurement the experimental error is given by 5% of the measurement value plus 5% of the maximal value of all included cells. For model fitting, we used the MATLAB solver lsqnonlin, to minimize residuals between measurements

$$r = \left(\frac{\tilde{I}_{il,data} - \tilde{I}_{il}}{\varepsilon(\tilde{I}_{il,data})} \right)^2 \quad (15)$$

for all cells. After initial fittings, parameter intervals were defined for $\tilde{\alpha}_{meta,il}$, $\tilde{\alpha}_{segr,il}$, $d_{meta,i}$ and $d_{segr,i}$ between 10^{-3} and 10^2 , and for β_{ij} between 10^{-7} and 10^2 . To accelerate convergence of model fits, parameters were fitted on a log-scale.

First, we started with fitting a model that only accounts for known literature interactions that were extracted from the *Ingenuity* pathway knowledge (IPA) database. To this end, β_{ij} was reduced to entries according to this set of literature interactions regarded as ground truth. Then, by sequential feature selection, additional affinities between proteins were further included if they could significantly improve the squared sum of residuals of the model fit. For each selection step of testing whether an additional interaction should be included, we performed 50 multi-start local optimizations by sampling initial conditions from allowed parameter intervals. We assured that after

optimizations, differences between the best fits were below the residuals for single data points. Additional entries in β_{ij} were selected based on likelihood-ratio testing, assuming that the likelihood-ratio for a model including an additional variable compared to a model without the additional parameter follows a one-dimensional χ^2 distribution. An additional affinity between proteins was included in β_{ij} if the increase in log-likelihood exceeded the 95% confidence interval of the cumulative one-dimensional χ^2 distribution. Following this forward selection procedure, 16 additional affinities between proteins were included. The reduction of the residual sum of squares is shown in **Supplementary Note Figure 2**.

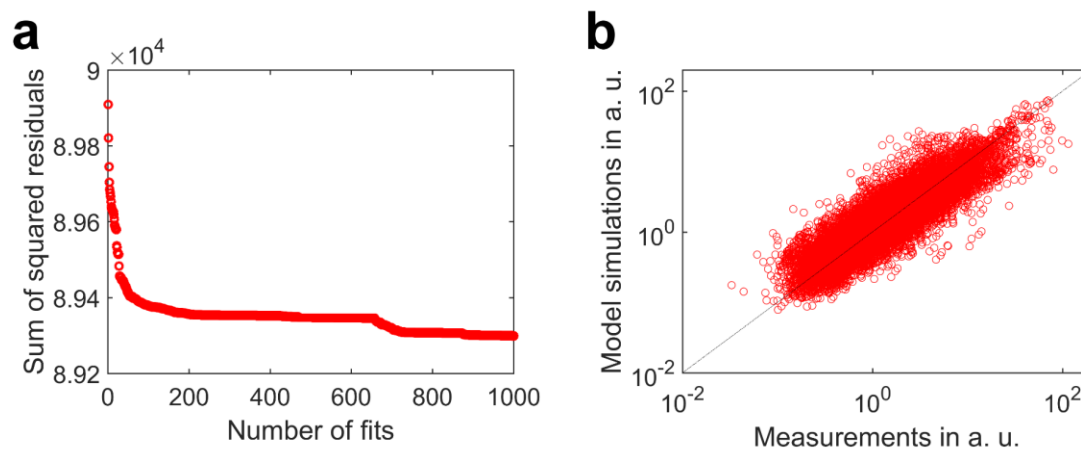


Supplementary Note Figure 2 Affinities between proteins included in addition to literature interactions. By sequential forward selection, entries in the matrix β_{ij} that contains mutual affinities between proteins were included in the model if the model fit was significantly improved. All included affinities were ordered according to the improvement in the χ^2 measure of model deviation from the experimental data.

These additional entries in β_{ij} represent hypotheses about mutual binding between proteins. Notably, this predicted mutual binding may be distinct from possible functional interactions between proteins. Mutual affinity does not necessarily imply a functional interaction, whereas a functional interaction may not require high binding affinity. Nevertheless, predictions of mutual affinities between the observed proteins involved in mitosis can be used

to guide further experiments for investigating functional relations and protein complexes that are linked to cellular processes.

After identifying an optimal set of additionally included affinities from model fitting to the control dataset, the model was fitted to data from inhibitor treatments. For every inhibitor treatment, the parameters $d_{meta,i}$, $d_{segr,i}$, $\tilde{\alpha}_{meta,il}$, $\tilde{\alpha}_{segr,il}$ and the extended β_{ij} were estimated by model fitting.



Supplementary Note Figure 3 Results of multi-start local optimizations. **(a)** Ordered sums of squared residuals for 1000 model fits to the control dataset from untreated cells. Differences between best fits were below the range of squared residuals for single data points indicating convergence of model fits towards a global optimum. **(b)** Best-fit model simulations and measurements indicate that the model is consistent with the experimental dataset.

Finally, to estimate effects from inhibitor treatments on compartment affinities and on mutual affinities between proteins, we again fitted the model to the control dataset from untreated cells and to datasets from inhibitor treatments. We performed in each case 1000 multi-start local optimizations by sampling initial conditions from allowed parameter intervals. **Supplementary Note Figure** shows the ordered sum of squared residual values for 1000 multi-start local optimization runs for fitting the control dataset. In **Supplementary Note Figure 3b** model simulations for the best model fit to the control dataset were plotted against experimental data. It is evident that the model fit is highly consistent with experimental measurements. Known and additionally predicted entries of β_{ij} , and estimated affinity values for the control dataset were shown in **Fig. 3c** and **3d**. Estimated affinity values for an exemplary inhibitor (PLK1) were visualized in **Fig. 3e**. Furthermore, the average affinities for all inhibitors were

shown in **Supplementary Fig. 2**. **Supplementary Fig 2c** shows estimates $\tilde{\alpha}_{meta,il}$, $\tilde{\alpha}_{segr,il}$ for estimated affinities to subcellular compartments, whereas **Supplementary Fig 2d** shows estimates $\alpha_{meta,il}/s_i$ and $\alpha_{segr,il}/s_i$ that were obtained by multiplying with scaling factors $d_{meta,i}$ and $d_{segr,i}$.